

Directionally asymmetric nonlinear optics in planar chiral MnTiO₃

Xinshu Zhang,^{1,*} Tyler Carbin,¹ Kai Du,² Bingqing Li,² Kefeng Wang,²
Casey Li,¹ Tiema Qian,¹ Ni Ni,¹ Sang-Wook Cheong,² and Anshul Kogar^{1,†}

¹*Department of Physics and Astronomy, University of California Los Angeles, Los Angeles, CA 90095, USA*

²*Rutgers Center for Emergent Materials, Rutgers University, Piscataway, NJ, USA*

(Dated: October 25, 2024)

Planar chiral structures possess a two-dimensional handedness that is associated with broken mirror symmetry. Such motifs span vast length scales; examples include certain pinwheel molecules, nautilus shells, cyclone wind patterns and spiral galaxies. Although pervasive in nature, it has only recently been found that condensed matter systems can exhibit a form of planar chirality through toroidal arrangements of electric dipoles, known as ferro-rotational (FR) order. A key characteristic of such order is that enantiomorph conversion occurs when the solid is flipped by 180 degrees about an in-plane axis. Consequently, ferro-rotationally ordered materials may exhibit directionally asymmetric response functions, even while preserving inversion and time-reversal symmetry. Such an effect, however, has yet to be observed. Using second harmonic interferometry, we show here that when circularly polarized light is incident on MnTiO₃, the generated nonlinear signal exhibits directional asymmetry. Depending on whether the incident light is parallel or anti-parallel to the FR axis, we observe a different conversion efficiency of two right (left) circularly polarized photons into a frequency-doubled left (right) circularly polarized photon. Our work uncovers a fundamentally new optical effect in ordered solids and opens up the possibility for developing novel nonlinear and directionally asymmetric optical devices.

Directional asymmetry (DA) refers to the breakdown of equivalence between the forward and backward direction of a physical process. Such asymmetry is present at the most fundamental levels of nature through the parity-violating weak interaction and also manifests itself at various other scales [1–5]. Examples include the Faraday effect, diode effect and magneto-chiral anisotropy effects, all of which give rise to the asymmetric propagation of electromagnetic signals [6–11]. In addition to their scientific importance, directional phenomena underpin devices such as semiconducting and superconducting diodes, optical isolators, circulators and acoustic gyrators [12–20]. In all of these cases, directional asymmetry arises in the presence of broken inversion (\mathcal{I}) and/or time-reversal (\mathcal{T}) symmetry, but DA does not require these symmetries to be broken.

A fundamental question, therefore, is if a condensed matter system possessing appropriate order can support DA without breaking \mathcal{I} or \mathcal{T} -symmetry. Because planar chiral structures exhibit a sense of twist that switches when viewed from the opposite direction (Fig. 1(a)), a material hosting such a structure should exhibit a directionally asymmetric effect. Pioneering works on engineered metamaterial structures possessing planar chirality have demonstrated the asymmetric transmission of circularly polarized microwaves [21–25]. Since previous studies focused exclusively on two-dimensional metamaterials that were manually patterned with a specific twofold rotational symmetry axis, it remains unclear whether an analogous effect can be observed in a spontaneously ordered three-dimensional solid. In this work, we show that materials hosting ferro-rotational (FR) order are ideal platforms for realizing DA without broken \mathcal{I} or \mathcal{T} symmetry.

To demonstrate the DA effect, we study the ferro-rotationally ordered compound MnTiO₃. At room temperature, the crystal structure of MnTiO₃ is represented by the centrosymmetric point group $\bar{3}$. Mn²⁺ and Ti⁴⁺ ions in the buckled honeycomb layers are stacked alternately along the z axis [26–32]. Rotational distortions of oxygen cages around the Mn²⁺ and Ti⁴⁺ ions break the {110} mirror plane symmetry, which results in a toroidal arrangement of electric dipole moments, i.e. ferro-rotational order (Fig. 1 (a)). In contrast to most ferro-rotational materials, which possess domains, MnTiO₃ naturally crystallizes in a single domain crystal which allows for unambiguous detection of directional asymmetry [31, 33–37]. To reduce further experimental complexity, we restrict our investigation to temperatures above the Néel temperature ($T_N=67$ K) [27–31].

At present, most known ferro-rotationally ordered materials possess threefold rotational symmetry about the FR axis which forbids the asymmetric transmission of linear optical signals [31, 33–37]. However, by extending the probe light into the nonlinear optical regime, we demonstrate that directional asymmetry of circularly polarized light can nevertheless be observed. We investigate MnTiO₃ with second harmonic generation (SHG), a process that converts two photons at frequency ω into one photon at frequency 2ω [38–40]. MnTiO₃ possesses inversion symmetry, which forbids the lowest order electric dipole contribution to SHG. The sub-leading contributions, magnetic dipole and electric quadrupole SHG, are

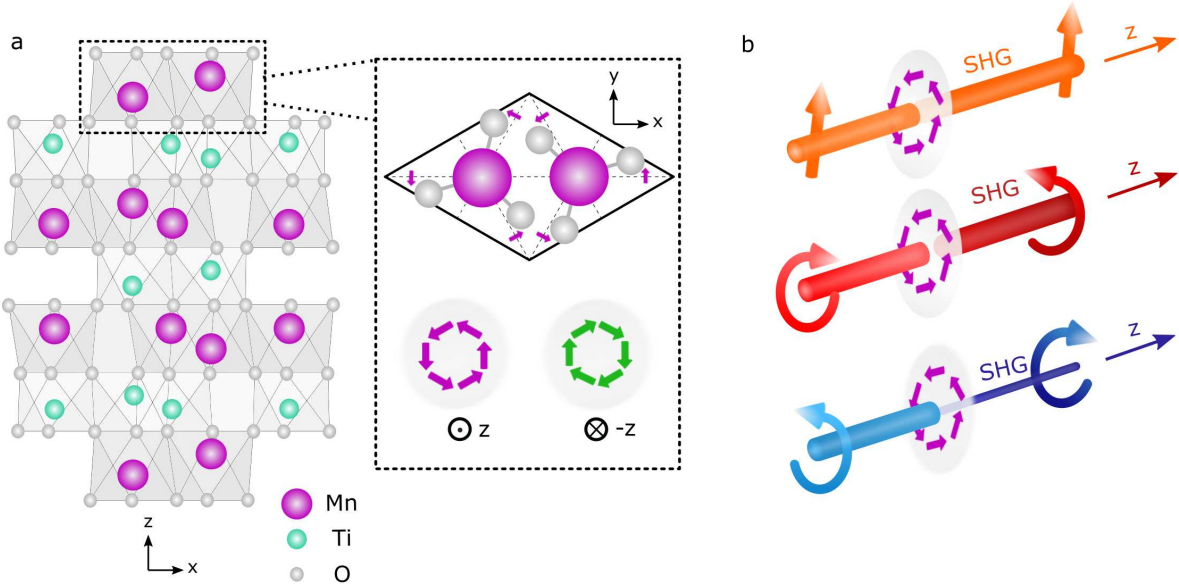


FIG. 1: (a) The crystal structures of MnTiO_3 with a ferro-rotational space group ($R\bar{3}$). The buckled honeycomb layers consisting of Mn^{2+} and Ti^{4+} ions are stacked alternately along z axis. Two oxygen cages enclosing two Mn^{2+} ions are enlarged and the top view is shown. Purple arrows denote the direction of rotational distortions of oxygen ions from the $\{110\}$ planes (dotted lines), breaking the mirror symmetry. The oxygen rotational displacements can be considered as planar chiral structures. The orientation of the FR order is counter-clockwise when viewing the structure along z direction, but switches to the clockwise orientation if viewed from the $-z$ direction. (b) Schematic of second harmonic generation experiments, which include RA-SHG and C-SHG. For RA-SHG the incident and outgoing beam are linearly polarized along the same axis. For C-SHG, the incident and outgoing beam are circularly polarized with opposite helicities.

both allowed and cannot be distinguished in our experiment; for simplicity, we refer only to magnetic dipole SHG in the remainder of the text.

To boost this usually weak signal, we tune the wavelength of the fundamental light between 960 and 1030 nm so that the SHG energy resonates with d - d transitions in the energy range spanning 2.4-2.6 eV [30, 38]. In the ferro-rotational state, two independent susceptibility tensor elements are permitted, $\chi_{yyy} = -\chi_{yxx} = -\chi_{xyx} = -\chi_{xxy}$ and $\chi_{xxx} = -\chi_{xyy} = -\chi_{yxy} = -\chi_{yyx}$, but only the χ_{yyy} -based terms are proportional to the ferro-rotational order parameter such that $\chi_{yyy}(\mathbf{L}) = -\chi_{yyy}(-\mathbf{L})$, where \mathbf{L} is the order parameter [30, 31, 33, 41] (Supplementary Note I). The presence of both terms, with only χ_{yyy} dependent on the sign of \mathbf{L} , ensures sensitivity to the orientation of the FR order through interference. The relative magnitudes and phases of χ_{xxx} and χ_{yyy} can be extracted by rotational anisotropy second harmonic generation (RA-SHG). In our experiment, the incident fundamental and detected second harmonic light are linearly polarized along the same direction. Once the relevant parameters have been extracted, we then perform circularly polarized second harmonic generation (C-SHG) with light propagating along the toroidal axis to illustrate intensity contrast between left and right circularly polarized light as well as the directional asymmetry effect.

To quantify the tensor elements, we first present RA-

SHG measurements as a function of temperature at a wavelength of 1005 nm (Fig. 2(a)). (RA-SHG patterns at a greater number of temperature points are shown in Supplementary Note III). The RA pattern at all temperatures can be fit with a simple expression (Supplementary Note I):

$$I(2\omega) \propto |\chi_{xxx}\sin(3\theta) + e^{i\gamma}\chi_{yyy}\cos(3\theta)|^2 \quad (1)$$

where χ_{xxx} and χ_{yyy} are the real-valued magnetic dipole tensor elements, γ denotes the relative phase between the two tensor elements and θ represents the polarization angle of the incident and detected light with respect to the x axis in MnTiO_3 (Fig. 1 (a)). At room temperature, the magnitude of χ_{yyy} is negligible compared to χ_{xxx} and the RA-SHG pattern exhibits almost perfect nodes (Supplementary Note II). As the temperature is lowered, the magnitude of χ_{yyy} increases. Consequently, the RA pattern rotates counterclockwise away from the crystal axes and the nodes are lifted as shown in Fig. 2 (a). The lifted nodes shrink again at low temperatures because χ_{yyy} becomes significantly larger than χ_{xxx} . By fitting the RA-SHG patterns, we can extract the magnitudes of χ_{xxx} and χ_{yyy} in addition to the relative phase as a function of temperature (Fig. 2 (b)-(c)).

The χ_{xxx}/χ_{yyy} ratio and the relative phase γ depend not only on the temperature, but also sensitively on the wavelength of the incident light. By scanning the incident light over a wavelength of 960-1030 nm, which

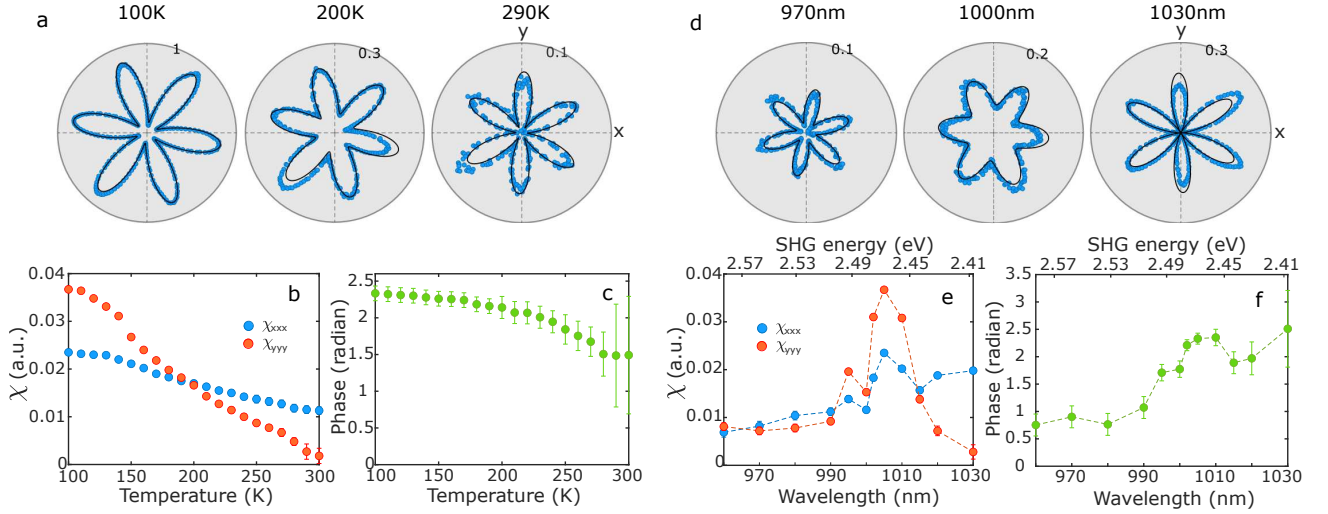


FIG. 2: (a) RA-SHG patterns with incident light wavelength 1005 nm at 100, 200 and 290 K. The intensities of all datasets are normalized to a value of 1 corresponding to 100 K. (b) χ_{xxx} (blue) and χ_{yyy} (red) as a function of temperature from 100 K to 300 K. (c) The relative phase γ between χ_{xxx} and χ_{yyy} as a function of temperature. (d) RA-SHG patterns for three selected incident wavelengths 970, 1000 and 1030 nm at 100 K. The intensities of all datasets are normalized to a value of 1 corresponding to 1005 nm at 100 K. (e) χ_{xxx} and χ_{yyy} as a function of wavelength from 960 to 1030 nm. (f) The relative phase γ between χ_{xxx} and χ_{yyy} as a function of wavelength. The error bars represent the standard deviation from the fit.

corresponds to a ${}^6A_{1g} \rightarrow {}^4T_{2g}$ crystal field transition, γ changes from roughly $\pi/4$ to $3\pi/4$, while χ_{xxx} and χ_{yyy} also change significantly (Fig. 2 (e)-(f)). Consequently, the RA-SHG patterns also adjust accordingly as shown in Fig. 2 (d) (more RA-SHG patterns at various wavelengths are shown in Supplementary Note IV). Over our experimental range of wavelengths and temperatures, the relative phase does not switch sign, which, as we show below, would correspondingly invert the contrast between left and right circularly polarized light. Nevertheless, it should be noted that nothing forbids such a phase change, and over a different energy range, this contrast may be reversed.

Because of the aforementioned interference, left and right circularly polarized light generate the second harmonic at different efficiencies. The efficiencies sensitively depend on the temperature and wavelength as shown in Figs. 3 (a) and (c). SHG intensity contrast between left and right circularly polarized incident light is shown in Figs. 3 (b) and (d). When the incident wavelength is 1005 nm, the contrast is not visible at room temperature within our experimental signal-to-noise ratio because the magnitude of χ_{yyy} is small compared to χ_{xxx} . But as χ_{yyy} becomes of equal magnitude to χ_{xxx} at roughly 200 K (Fig. 2 (b)), the contrast is maximal (Fig. 3 (b)). Understanding this disparity requires converting Eq. 1 to the circular basis:

$$\begin{aligned} I_L(2\omega) &\propto |i\chi_{xxx} + e^{i\gamma}\chi_{yyy}|^2 I_R^2(\omega) \\ I_R(2\omega) &\propto |i\chi_{xxx} - e^{i\gamma}\chi_{yyy}|^2 I_L^2(\omega). \end{aligned} \quad (2)$$

From these expressions, it is clear that the contrast between the right and left circularly polarized light is ob-

servable only when the matrix elements are of comparable magnitude and when $\gamma \neq m\pi$, where m is an integer. In correspondence with the RA patterns, the cir-

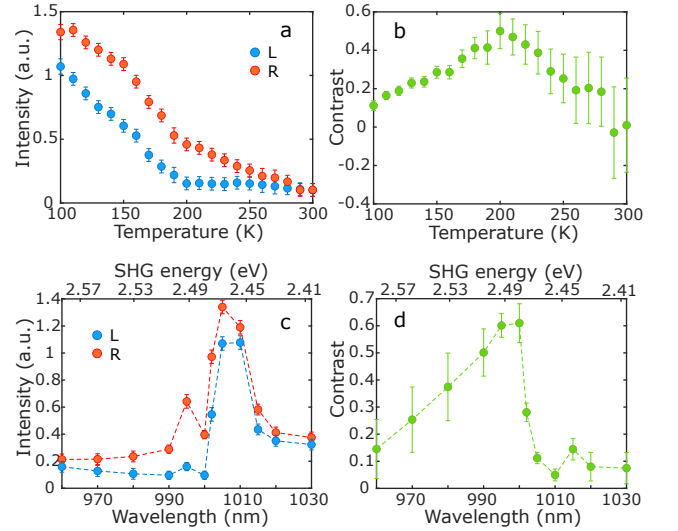


FIG. 3: (a) The intensity of C-SHG as a function of temperature for incident light with left (L) and right (R) circular polarization at an incident wavelength of 1005 nm. (b) The temperature dependent C-SHG contrast defined as $(R-L)/(R+L)$, highlighting the different efficiencies for left and right circularly polarized incident light. (c) The intensity of C-SHG as a function of wavelength for incident light with left (L) and right (R) circular polarization at $T = 100$ K. (d) The wavelength dependent C-SHG contrast. The error bars represent the standard deviation from two independent measurements.

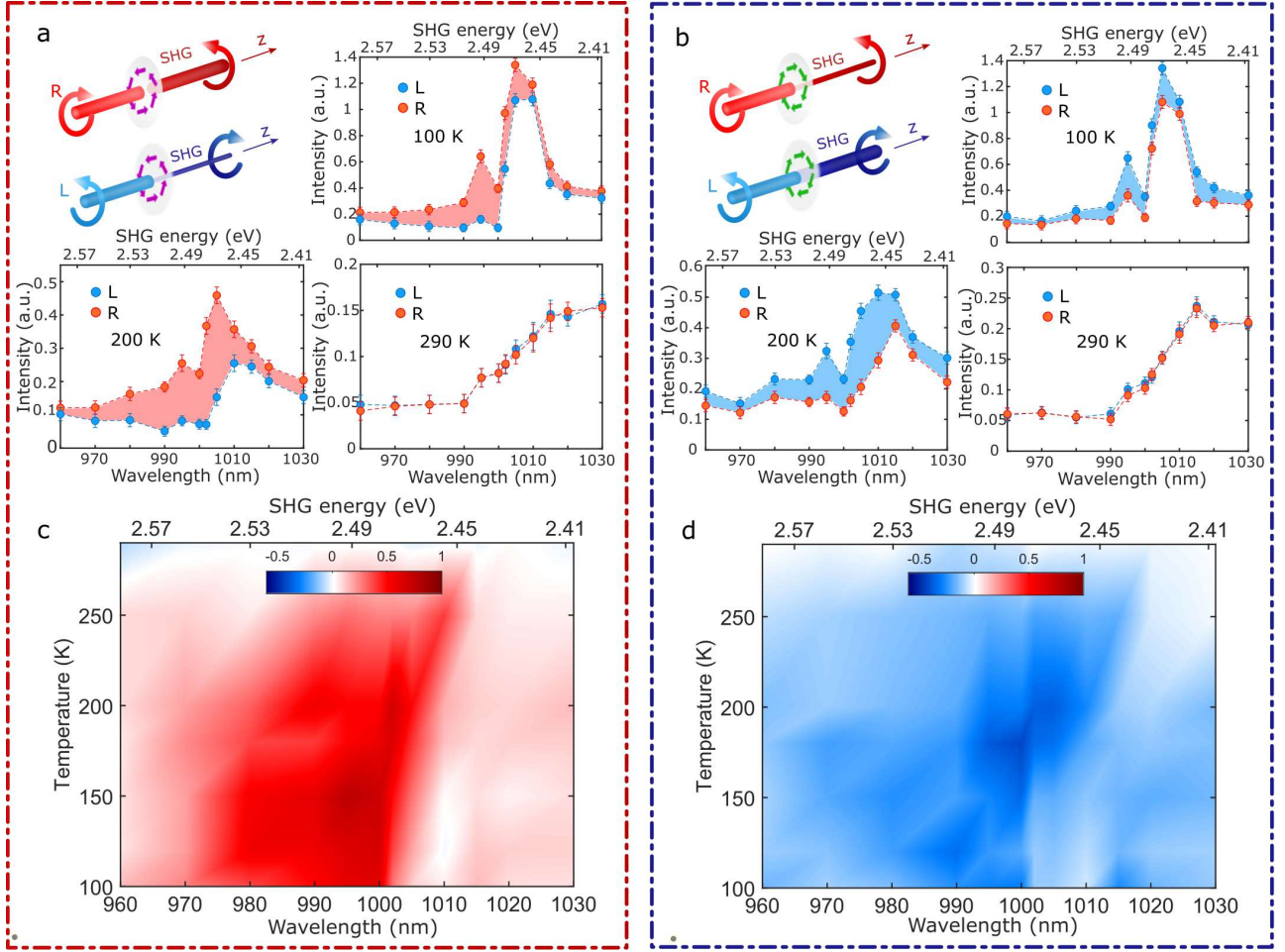


FIG. 4: (a)-(b) Wavelength dependent C-SHG for two planar chiral structures at 100 K, 200 K and 290 K. The error bars represent the standard deviation from two independent measurements. (c)-(d) Color plots depicting the normalized SHG intensity contrast between left and right circularly polarized incident light as a function of temperature and wavelength for two planar chiral structures.

circularly polarized contrast is most pronounced when the node is maximally lifted. At 100 K, when the wavelength is tuned between 995-1000 nm, $\gamma \approx \pi/2$ and $|\chi_{xxx}| \approx |\chi_{yyy}|$, which means that primarily left circularly polarized second harmonic light is generated, while right circularly polarized light is hardly produced. The contrast is thus maximal at this point, as shown in Figs. 3 (d). It is important to note that while the contrast between left and right circularly polarized light is necessary to observe the directional asymmetry effect, it is not a sufficient condition (e.g. circularly polarized SHG contrast is observed in Cr_2O_3 without directional asymmetry) [42–44].

The presence of directional asymmetry in the ferro-rotational state of MnTiO_3 is illustrated in Fig. 4. In Fig. 4 (a), wavelength-dependent C-SHG is shown for one planar chiral structure at 100 K, 200 K and 290 K, while Fig. 4 (b) shows the results for the other enantiomorph by flipping the sample 180 degrees about an in-plane axis.

Flipping the sample in this way is equivalent to reversing the positions of the source and detector and therefore comprises a test of directional asymmetry. Prior to flipping the sample, we observe a higher second harmonic conversion efficiency for right circularly polarized light, whereas afterwards, the same is true of left circularly polarized light. As expected from the tensor elements and relative phase extracted from the RA-SHG, the DA contrast is largest at around 200 K, while asymmetry can still be observed at 100 K. At 290 K, however, because χ_{yyy} is negligibly small compared to χ_{xxx} , we do not observe contrast between left and right circularly polarized light; subsequently, the directional asymmetry effect disappears. This observation illustrates that the directional asymmetry effect arises due to interference between tensor elements that are proportional to the order parameter and elements that are not. Only the χ_{yyy} -based elements change sign upon rotating the sample, while the χ_{xxx} terms provide an unchanged reference. Figs. 4 (c)

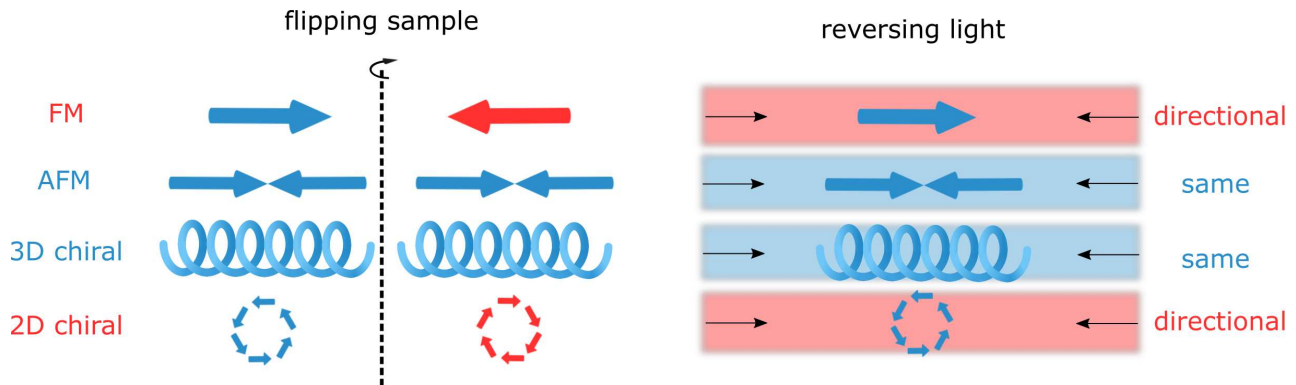


FIG. 5: Four representative systems are chosen to illustrate the conditions required for directional asymmetry, including a ferromagnet (FM), an anti-ferromagnet (AFM), a three dimensional (3D) chiral system and a planar (2D) chiral system. Due to the lack of in-plane C_2 symmetry, flipping the FM and the planar chiral system results in distinct properties (e.g., the spin direction reverses in the FM while a counter-clockwise rotation switches to a clockwise rotation for a planar chiral system). Consequently, circularly polarized light propagating in opposite directions interact differently with these material systems. In contrast, in AFMs and 3D chiral systems, which preserve C_2 symmetry and remain unchanged upon flipping, the same electromagnetic response is observed regardless of the direction of propagation.

and (d) summarize the directional effect as a function of wavelength and temperature, revealing a clear directional asymmetry across nearly the entire range of the relevant phase space.

To understand the general requirements for observing the DA effect with circularly polarized light, one must consider the roles played by symmetry and angular momentum transfer. Crucially, twofold rotational symmetry about any axis perpendicular to the FR axis must be broken. Colloquially stated, it is imperative that flipping the sample over will not leave the crystal invariant. As we show in Fig. 5, this constraint is also obeyed by Faraday media, which also exhibit directional asymmetry in the propagation speed of circularly polarized light. On the other hand, simple collinear anti-ferromagnetic systems (like Cr_2O_3) and three dimensional chiral systems, which possess a twofold in-plane rotational symmetry axis, exhibit the same response for counter-propagating light waves [42–45]. However, the absence of this rotational axis is not the only relevant broken symmetry. Specifically, all mirror planes that contain the FR axis must also be broken. The presence of such mirror symmetries would prevent a preference for one circular polarization over the other, which is essential for the observed effect. Notably, neither inversion symmetry nor time-reversal symmetry need to be absent; the relevant twofold rotation and mirror operations are the primary symmetries to be considered for observing the DA effect presented here.

Whether one observes this DA effect within the realm of linear or nonlinear optics depends on considerations related to angular momentum conservation. An important aspect of Eq. 2 is that two left (right) circularly polarized incident photons are converted into one right (left) circularly polarized second harmonic photon. Each circularly

polarized photon carries an angular momentum of $\pm\hbar$; an incident photon will transfer this amount to a solid, while an outgoing photon will carry it away. Thus, the conversion of photons from right (left) circularly polarized light to left (right) circularly polarized light entails elastically transferring angular momentum to the solid. Such a process is analogous to that of Bragg diffraction from a crystal, where linear momentum (but not energy) is transferred. The amount of angular momentum that can be transferred to the solid with circularly polarized light depends on the rotational symmetry of the crystal about the propagation axis [46, 47]. As established in Ref. [46], integer multiples of $n\hbar$ units of angular momentum, where n is an integer, can be transferred to a crystal when the light propagates along an n -fold rotational symmetry axis. In the case of MnTiO_3 , where light propagates along a threefold symmetric rotation axis, the process in which two right (left) circularly polarized photons incident on the crystal produce a single outgoing left (right) circularly polarized photon at twice the frequency (which transfers $\pm 3\hbar$ units of angular momentum to the solid) is therefore allowed. Consequently, the directional asymmetry effect in MnTiO_3 cannot be observed in a linear optical experiment, which would require the FR axis to be a twofold rotational symmetry axis. A second order nonlinear optical process is thus the key to the helicity conversion of circularly polarized photons and underlies the directional asymmetry effect in MnTiO_3 .

Our observations demonstrate that directional asymmetry of circularly polarized light can be realized in a system without broken \mathcal{I} or \mathcal{T} -symmetry in ferro-rotational MnTiO_3 . We predict that solids sharing a twofold rotational symmetry axis and a toroidal axis due to ferro-rotational order should exhibit a directionally asymmetric conversion efficiency of circularly polarized light with-

out invoking nonlinear optics. Furthermore, engineered two-dimensional materials with Moire superstructures that produce planar chiral motifs also offer promising avenues through which to investigate directionally asymmetric propagation of circularly polarized light [48–50]. Our findings pave the way for the search of directional asymmetry in other unconventional structures and expand the material database for the development of novel linear and nonlinear optical devices.

ACKNOWLEDGEMENTS:

We thank Xianghan Xu and Boxuan Zhou for helpful conversations related to this work. We thank Jonathan Loera and J Green for the help in X-ray diffraction measurements. The SHG experiments at UCLA were supported by the U.S. Department of Energy (DOE), Office of Science, Office of Basic Energy Sciences under Award No. DE-SC0023017. N.N. and T.Q. were supported by the U.S. Department of Energy (DOE), Office of Science, Office of Basic Energy Sciences under Award Number DE-SC0021117. The work at Rutgers was supported by W. M. Keck Foundation.

AUTHOR CONTRIBUTIONS:

X.Z. performed the RA-SHG and C-SHG experiments with the help from T.C. and C.L.. X.Z. analysed the data. The SHG project was performed under the supervision of A.K.. K.D., B.L. and K.W. grew the single crystals under the supervision of S.-W.C.. T.Q. and N.N. prepared the crystal for measurements and characterized the crystal with X-ray diffraction. The manuscript was written by X.Z. and A.K. with input from all authors.

COMPETING INTERESTS:

The authors declare no competing interests.

METHODS

Sample synthesis

MnO (Thermo Scientific, 99.99%) and TiO₂ (Alfa Aesar, 99.8%) powder were mixed at the stoichiometric ratio and calcined in air from 1000°C to 1400°C with intermediate grindings at each 100°C interval. The powder was then made into feed-rods that has been hydrostatically pressed at 800 bar and sintered at 1400°C for 20 hours. Single crystals of MnTiO₃ were grown in the laser floating-zone furnace (Crystal System Corporation, Japan) where the feed-rods were grown at 3 mm/h in Argon with ambient pressure and both feed and seed rods were counter-rotated at rates around 18 rpm.

Experimental details

The regeneratively amplified laser used in our experiment is based on a Yb:KGW gain medium that outputs a power of 10 W. The laser pulses have a Gaussian-like profile with an approximately 180 fs pulse duration and a 1030 nm central wavelength. In our experiment, we used a laser pulse repetition rate of 20 kHz. The laser pulse was generated from an optical parametric amplifier with

tunable wavelength, which we use for the second harmonic spectroscopy between 960-1030 nm. The laser pulse was focused normally on the sample with a 100 μm spot size, and the probe fluence was approximately 15 mJ/cm². Detection of the second harmonic light was conducted with a commercial photo-multiplier tube. The sample was cooled with a standard optical cryostat with fused silica windows to prevent distortions to the light polarization.

DATA AVAILABILITY

The data that supports the findings of this study are present in the paper and/or in the supplementary information, and are deposited in the Zenodo repository. Additional data related to the paper is available from the corresponding authors upon reasonable request.

* Electronic address: xszhang@physics.ucla.edu

† Electronic address: anshulkogar@physics.ucla.edu

- [1] Tokura, Y. & Nagaosa, N. Nonreciprocal responses from non-centrosymmetric quantum materials. *Nat. Commun.* **9**, 3740 (2018)
- [2] Caloz, C. et al. Electromagnetic Nonreciprocity. *Phys. Rev. Applied* **10**, 047001 (2018)
- [3] Potton, R. Reciprocity in optics. *Rep. Prog. Phys.* **67**, 717–754 (2004)
- [4] Cheong, S. et al. Broken symmetries, non-reciprocity, and multiferroicity. *npj Quantum Mater.* **3**, 19 (2018)
- [5] Wu, C. et al. Experimental Test of Parity Conservation in Beta Decay. *Phys. Rev.* **105**, 1413 (1957)
- [6] Faraday, M. On the magnetization of light and the illumination of magnetic lines of force. *Phil. Trans. R. Soc.* **136**, 1-20 (1846)
- [7] Rikken, G. & Raupach, E. Observation of magneto-chiral dichroism. *Nature* **390**, 493–494 (1997)
- [8] Rikken, G. et al. Electrical Magnetochiral Anisotropy. *Phys. Rev. Lett.* **87**, 236602 (2001).
- [9] Tzschaschel, C. et al. Nonlinear optical diode effect in a magnetic Weyl semimetal. *Nat. Commun.* **15**, 3017 (2024).
- [10] Toyoda, S. et al. Nonreciprocal second harmonic generation in a magnetoelectric material. *Sci. Adv.* **7**, eabe2793 (2021).
- [11] Shoriki, K. et al. Large nonlinear optical magnetoelectric response in a noncentrosymmetric magnetic Weyl semimetal. *Proc. Natl. Acad. Sci.* **121**, e2316910121 (2024).
- [12] Fan, L. et al. An All-Silicon Passive Optical Diode. *Science* **335**, (6067) 447-450 (2011)
- [13] Pospischil, A. et al. Solar-energy conversion and light emission in an atomic monolayer p–n diode. *Nat. Nanotechnol* **9**, 257–261 (2014)
- [14] Ando, F. et al. Observation of superconducting diode effect. *Nature* **584**, 373–376 (2020)
- [15] Nassar, H. et al. Nonreciprocity in acoustic and elastic materials. *Nat. Rev. Mater.* **5**, 667–685 (2020)
- [16] Jalas, D. et al. What is and what is not an optical isolator. *Nat. Photon.* **7**, 579–582 (2013)
- [17] Tian, H. et al. Magnetic-free silicon nitride integrated optical isolator. *Nat. Photon.* **15**, 828–836 (2021)
- [18] White, A. et al. Integrated passive nonlinear optical isolators. *Nat. Photon.* **17**, 143–149 (2023)

- [19] Shen, Z. et al. Experimental realization of optomechanically induced non-reciprocity. *Nat. Photon.* **10**, 657–661 (2016)
- [20] Fleury, R. et al. Sound Isolation and Giant Linear Nonreciprocity in a Compact Acoustic Circulator. *Science* **343**, 516–519 (2014)
- [21] Fedotov, V. et al. Asymmetric Propagation of Electromagnetic Waves through a Planar Chiral Structure. *Phys. Rev. Lett.* **97**, 167401 (2006).
- [22] Zheludev, N. & Kivshar, Y. From metamaterials to metadevices. *Nat. Mater.* **11**, 917–924 (2012).
- [23] Schwanecke, A. et al. Nanostructured metal film with asymmetric optical transmission. *Nano Lett.* **8**, 2940–2943 (2008).
- [24] Plum, E. et al. Planar metamaterial with transmission and reflection that depend on the direction of incidence. *Appl. Phys. Lett.* **94**, 131901 (2009).
- [25] Papakostas, A. et al. Optical Manifestations of Planar Chirality. *Phys. Rev. Lett.* **90**, 107404 (2003).
- [26] Kidoh, K. et al. Electron density distribution in ilmenite-type crystals. II. Manganese(II) titanium(IV) trioxide. *Acta. Crystallogr., Sect. B* **40**, 329 (1984).
- [27] Maurya, R. et al. Evidence of spin lattice coupling in MnTiO₃: An x-ray diffraction study. *Europhysics Letters* **110**, 27007 (2015).
- [28] Sato, T. et al. Magnetochiral Dichroism in a Collinear Antiferromagnet with No Magnetization. *Phys. Rev. Lett.* **124**, 217402 (2020).
- [29] Sato, T. et al. Antiferromagnetic domain wall dynamics in magnetoelectric MnTiO₃ studied by optical imaging. *Phys. Rev. B* **105**, 094417 (2022).
- [30] Cherian, J. et al. Electronic structure and magnetic symmetry in MnTiO₃ analyzed by second harmonic generation. *Phys. Rev. B* **87**, 214411 (2013).
- [31] Sekine, D. et al. Second harmonic imaging of antiferromagnetic domains and confirmation of absence of ferroaxial twins in MnTiO₃. *Phys. Rev. Mater.* **8**, 064406 (2024).
- [32] Mufti, N. et al. Magnetoelectric coupling in MnTiO₃. *Phys. Rev. B* **83**, 104416 (2011).
- [33] Jin, W. et al. Observation of a ferro-rotational order coupled with second-order nonlinear optical fields. *Nat. Phys.* **16**, 42–46 (2020).
- [34] Hayashida, T. et al. Observation of a ferro-rotational order coupled with second-order nonlinear optical fields. *Nat. Commun.* **11**, 4582 (2020).
- [35] Yokota, H. et al. Three-dimensional imaging of ferroaxial domains using circularly polarized second harmonic generation microscopy. *npj quantum mater* **7**, 106 (2022).
- [36] Guo, X. et al. Ferrorotational domain walls revealed by electric quadrupole second harmonic generation microscopy. *Phys. Rev. B* **107**, L180102 (2023).
- [37] Du, Kai. et al. Kibble–Zurek mechanism of Ising domains. *Nat. Phys.* **19**, 1495–1501 (2023).
- [38] Fiebig, M., Pavlov, V. & Pisarev, R. Second-harmonic generation as a tool for studying electronic and magnetic structures of crystals: review *J. Opt. Soc. Am. B* **22**, 1, 96–118 (2005).
- [39] Boyd, R. Nonlinear optics. *Academic Press* (2020).
- [40] Powell, R. Symmetry, group theory, and the physical properties of crystals *Springer* (2010).
- [41] Birss, R. Symmetry and Magnetism. *North Holland*, (1966).
- [42] Zhang, X. et al. Light-induced electronic polarization in antiferromagnetic Cr₂O₃. *Nat. Mater.* **23**, 790–795 (2024).
- [43] Fiebig, M. et al. Second Harmonic Generation and Magnetic-Dipole —Electric-Dipole Interference in Antiferromagnetic Cr₂O₃. *Phys. Rev. Lett.* **73**, 2127 (1994).
- [44] Fiebig, M., Fröhlich, D. & Sluyterman, G. Domain topography of antiferromagnetic Cr₂O₃ by second-harmonic generation. *Appl. Phys. Lett.* **66**, 2906 (1995).
- [45] Barron, L. Parity and Optical Activity. *Nature* **238**, 17–19 (1972)
- [46] Simon, H. & Bloembergen, N. Second-Harmonic Light Generation in Crystals with Natural Optical Activity. *Phys. Rev.* **171**, 1104 (1968).
- [47] Sun, Z. et al. Giant nonreciprocal second-harmonic generation from antiferromagnetic bilayer CrI₃. *Nature* **572**, 497–501 (2019).
- [48] Novoselov, K. et al. 2D materials and van der Waals heterostructures. *Science* **253**, aac9439 (2016).
- [49] Mak, K. & Shan, J. Photonics and optoelectronics of 2D semiconductor transition metal dichalcogenides. *Nat. Photon.* **10**, 216–226 (2016).
- [50] Yang, H. et al. Visualization of Chiral Electronic Structure and Anomalous Optical Response in a Material with Chiral Charge Density Waves. *Phys. Rev. Lett.* **129**, 156401 (2022).

Supplementary Information for Directionally asymmetric nonlinear optics in planar chiral MnTiO₃

Xinshu Zhang,^{1,*} Tyler Carbin,¹ Kai Du,² Bingqing Li,² Kefeng Wang,² Casey Li,¹ Tiema Qian,¹ Ni Ni,¹ Sang-Wook Cheong,² and Anshul Kogar^{1,†}

¹*Department of Physics and Astronomy, University of California Los Angeles, Los Angeles, CA 90095, USA*

²*Rutgers Center for Emergent Materials, Rutgers University, Piscataway, NJ, USA*

(Dated: October 25, 2024)

I. ANALYSIS OF SHG

A. Rotational anisotropy SHG

Radiation can come from various sources, including electric dipoles, magnetic dipoles, electric quadrupoles, and higher order radiation sources. In MnTiO₃ above anti-ferromagnetic transition temperature $T_N = 67\text{K}$, the electric dipole contribution to SHG is forbidden due to inversion symmetry, while the magnetic dipole and electric quadrupole contributions are allowed. These two contributions give rise to the same expressions in our experimental geometry and therefore yield no additional information pertaining to the symmetry of the emitted radiation. Therefore, for simplicity, we neglect the electric quadrupole contribution and consider only the magnetic dipole SHG. The source term entering Maxwell's equations is then given by $\mathbf{S} = \nabla \times \frac{\partial \mathbf{M}}{\partial t}$. The magnetic contribution at the second harmonic frequency has the form of $\mathbf{M}(2\omega) = \chi \mathbf{E}(\omega) \mathbf{E}(\omega)$, where χ is the second order nonlinear magnetic susceptibility tensor, and \mathbf{E} is the incident electric field at the fundamental frequency. Above T_N , MnTiO₃ has point group $\bar{3}$. For light propagating along the z -direction (optical axis of the crystal), the magnetic susceptibility tensors have only two independent tensor elements with the relation $\chi_{yyy} = -\chi_{yxx} = -\chi_{xyx} = -\chi_{xxy}$ and $\chi_{xxx} = -\chi_{xyy} = -\chi_{yyx} = -\chi_{yxy}$. Therefore, the source term is given by:

$$\mathbf{S} \propto \nabla \times \frac{\partial \mathbf{M}}{\partial t} \propto \begin{pmatrix} \chi_{yyy}(E_x^2 - E_y^2) + 2\chi_{xxx}E_xE_y \\ \chi_{xxx}(E_x^2 - E_y^2) - 2\chi_{yyy}E_xE_y \\ 0 \end{pmatrix}. \quad (\text{S1})$$

The second harmonic intensity measured by the detector in our experiment is $I \propto |\mathbf{e}(2\omega) \cdot \mathbf{S}|^2$, where $\mathbf{e}(2\omega)$ is the unit vector of the output polarizer that selects second harmonic light of a particular polarization. By taking the polarization of both the incident fundamental light and the outgoing SHG light into account, we obtain

$$I(2\omega) \propto |\chi_{xxx} \sin(3\theta) + \chi_{yyy} \cos(3\theta)|^2, \quad (\text{S2})$$

where θ is taken to be with respect to the x -axis. χ_{yyy} and χ_{xxx} are complex quantities, but only the relative phase between them is important. We can rewrite the above expression as

$$I(2\omega) \propto |\chi_{xxx}| |\sin(3\theta) + e^{i\gamma} |\chi_{yyy}| \cos(3\theta)|^2, \quad (\text{S3})$$

The magnitude $|\chi_{yyy}|$, $|\chi_{xxx}|$ and relative phase γ can be obtained by fitting to the rotational anisotropy second harmonic generation (RA-SHG) patterns.

B. Circular SHG

In this section, we demonstrate that illuminating MnTiO₃ with left circularly polarized light results in the emission of right circularly polarized light at twice the frequency, and vice versa. This is a consequence of angular momentum conversion and the threefold rotational symmetry of the crystal about the z -axis of the crystal. We can convert the

*Electronic address: xszhang@physics.ucla.edu

†Electronic address: anshulkogar@physics.ucla.edu

source term from linear basis in S1 into circular basis with $\mathbf{E} = E_R \mathbf{e}_R + E_L \mathbf{e}_L + E_z \mathbf{e}_z$, where $\mathbf{e}_R = -1/\sqrt{2}(\mathbf{e}_x + i\mathbf{e}_y)$ and $\mathbf{e}_L = 1/\sqrt{2}(\mathbf{e}_x - i\mathbf{e}_y)$. Then one gets

$$\mathbf{S} = \begin{pmatrix} S_R \\ S_L \\ S_z \end{pmatrix} \propto \begin{pmatrix} (-\chi_{yyy} + i\chi_{xxx})E_L^2 \\ (\chi_{yyy} + i\chi_{xxx})E_R^2 \\ 0 \end{pmatrix} \quad (\text{S4})$$

$I_{R/L} \propto |\mathbf{S}|^2$. Hence, the circular SHG intensity is

$$\begin{aligned} I_L(2\omega) &\propto |\chi_{yyy} + i\chi_{xxx}|^2 I_R^2(\omega) \\ I_R(2\omega) &\propto |-\chi_{yyy} + i\chi_{xxx}|^2 I_L^2(\omega). \end{aligned} \quad (\text{S5})$$

Alternatively, we can express these expressions in terms of the magnitude and phase:

$$\begin{aligned} I_L &\propto (|\chi_{xxx}|^2 + |\chi_{yyy}|^2) + 2(|\chi_{xxx}||\chi_{yyy}|)\sin(\gamma) \\ I_R &\propto (|\chi_{xxx}|^2 + |\chi_{yyy}|^2) - 2(|\chi_{xxx}||\chi_{yyy}|)\sin(\gamma). \end{aligned} \quad (\text{S6})$$

The first term is quadratic in χ_{xxx} and χ_{yyy} , and is always positive, while the second term is the so-called interference term and can be either positive or negative. The sign of the interference term can be reversed by either changing the handedness of the circular light or by flipping the sample 180 degrees. Additionally, the interference is also affected by the wavelength of the light. The greatest contrast in the second harmonic response to the incident left and right circularly polarized light occurs when the χ_{xxx} and χ_{yyy} have equal magnitudes and possess a 90-degree phase difference.

II. ROOM TEMPERATURE RA-SHG

At room temperature, the magnitude of χ_{yyy} is negligible compared to χ_{xxx} . As a result, the RA-SHG patterns at various wavelengths all possess nodes. Additionally, the intensity maxima are aligned to the crystal axes. In contrast, at lower temperatures, χ_{yyy} grows and according to Eq. S4, the nodes can be lifted and the pattern can be rotated away from the crystal axes at various wavelengths depending on the χ_{xxx}/χ_{yyy} ratio. In Fig. S1, we show three representative RA-SHG patterns at 290 K. The slight rotation away from the y -axis for the 1000 nm pattern indicates the presence of a residual χ_{yyy} contribution due to the ferro-rotational order.

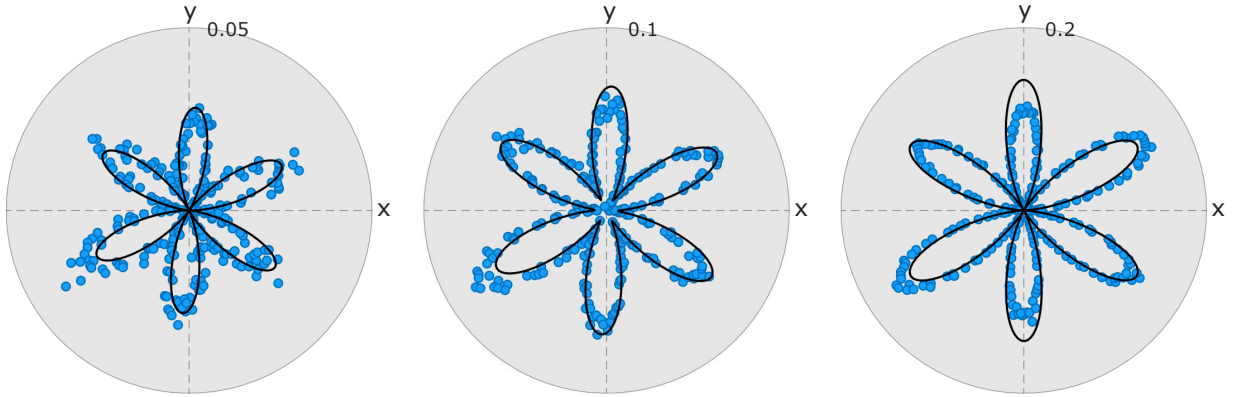


FIG. S1 RA-SHG at 290 K for 1000 nm (left), 1005 nm (middle) and 1030 nm (right).

III. TEMPERATURE DEPENDENCE OF SHG AT FIXED WAVELENGTH

In this section, we present the RA-SHG patterns at 1005 nm incident light, measured from 100 K to 290 K in 10 K increments.

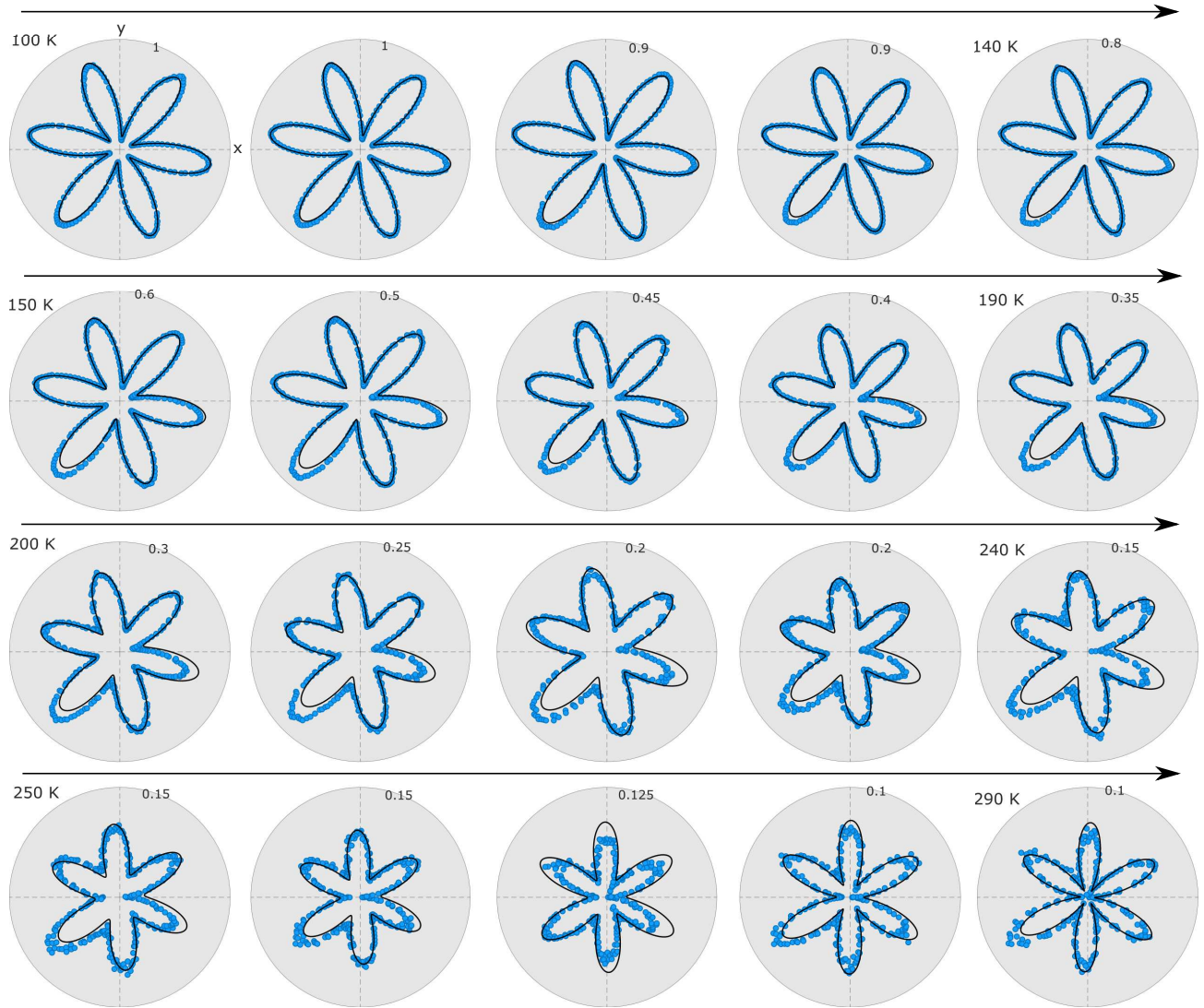


FIG. S2 RA-SHG for 1005 nm incident wavelength at various temperatures ranging from 100 K to 290 K. The top row displays RA-SHG from 100 K to 140 K, the second row from 150 K to 190 K, the third row from 200 K to 240 K and the bottom row from 250 K to 290 K (temperature increases from left to right for each row).

IV. WAVELENGTH DEPENDENCE OF SHG AT FIXED TEMPERATURE

In this section, we show RA-SHG patterns at 100 K for various incident wavelengths ranging from 960 nm to 1030 nm. The fundamental wavelengths of 960-1030 nm correspond to the SHG energies of 2.4-2.6 eV, which resonate with several $d-d$ transitions in MnTiO_3 . Across the crystal field transitions, the magnitude of χ_{xxx} and χ_{yyy} and the relative phase between them change drastically. Consequently, the patterns also change prominently with varying wavelength.

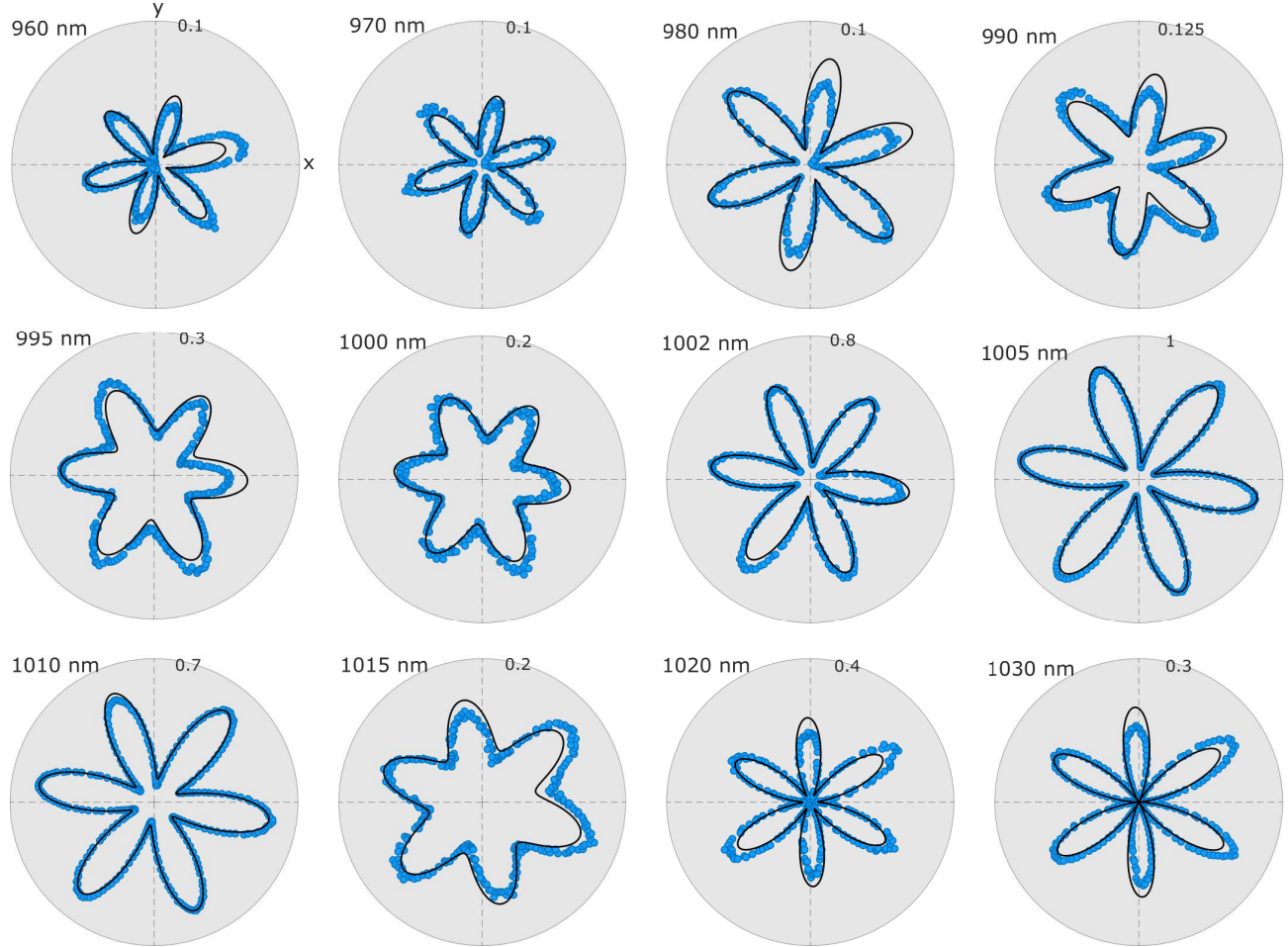


FIG. S3 RA-SHG at 100 K for various wavelengths from 960 nm to 1030 nm.